Journal of Power Sources 693 (2026) 241076

Contents lists available at ScienceDirect

Journal of Power Sources

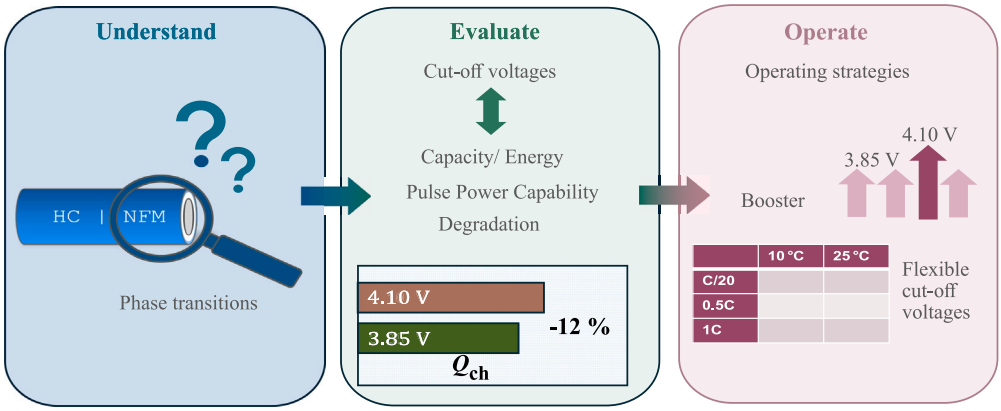
journal homepage: www.elsevier.com/locate/jpowsour

From analysis to operating strategy: Dealing with phase transitions in sodium-ion batteries

Andrea Kinberger [a,b,*], Tom Rüther [a,b], Niklas Feistel [a], Qingsong Wang [c,b], Matteo Bianchini [c,b], Michael A. Danzer [a,b]

[a] Chair of Electrical Energy Systems, University of Bayreuth, Universitätsstraße 30, Bayreuth, 95447, Bavaria, Germany
[b] Bavarian Center for Battery Technology, University of Bayreuth, Universitätsstraße 30, Bayreuth, 95447, Bavaria, Germany
[c] Chair of Inorganic Active Materials for Electrochemical Energy Storage, University of Bayreuth, Universitätsstraße 30, Bayreuth, 95447, Bavaria, Germany

GRAPHICAL ABSTRACT



HIGHLIGHTS

- Phase transitions indicated in cycling data are confirmed by operando-XRD.
- Determination of temperature and C-rate dependent onset of phase transition during cycling.
- Phase transition onset can guide the choice of the upper cut-off voltage.
- Impact of the voltage limit on capacity, energy, power capability, and cycle life is assessed.
- Operating strategies for balancing capacity, energy, and cycle life are proposed.

ARTICLE INFO

Keywords:
Sodium-ion battery
NFM
Phase transition
Upper cut-off voltage
Degradation mechanisms

ABSTRACT

Sodium-ion batteries are emerging as a sustainable and cost-effective alternative to lithium-ion batteries for large-scale stationary energy storage. However, a key challenge of layered oxide cathodes, such as $Na_xNi_yFe_zMn_{1-y-z}O_2$, is their structural instability under high-voltage operation. In particular, it is suspected that a voltage-induced phase transition accelerates degradation and limits long-term performance. This creates a central trade-off: expanding the voltage window is highly attractive from an application perspective, as it enables higher capacities and energy densities. However, it may also compromise cycle life by promoting structural degradation. In this study, we directly address this issue by linking the evolution of high-voltage

* Corresponding author at: Chair of Electrical Energy Systems, University of Bayreuth, Universitätsstraße 30, Bayreuth, 95447, Bavaria, Germany.
E-mail address: andrea.kinberger@uni-bayreuth.de (A. Kinberger).

https://doi.org/10.1016/j.jpowsour.2026.241076
Received 16 June 2026; Received in revised form 16 July 2026; Accepted 23 July 2026
Available online 6 August 2026
0378-7753/© 2026 The Authors. Published by Elsevier B.V. This is an open access article under the CC BY license (http://creativecommons.org/licenses/by/4.0/).

phase transitions to the practical performance limits of sodium-ion layered oxide cathodes. Operando X-ray diffraction combined with electrochemical cycling analysis is first used to establish a mechanistic understanding of how these phase transitions develop during cycling. We then systematically evaluate their occurrence as a function of temperature and C-rate, quantifying their impact on capacity, energy, and power capability. Long-term cycling further reveals the effect of high-voltage operation on cycle life. Based on these findings, we propose an operating strategy that balances the gains in initial capacity, energy output, and power capability with the degradation risks associated with high-voltage operation.

1. Introduction

Among emerging battery technologies, sodium-ion batteries (SIB) are considered a promising alternative to lithium-ion batteries (LIB). SIBs benefit from lower supply criticality, a higher natural abundance, a broader geographical availability, and potentially lower raw-material costs [1–3]. However achieving competitive performance and service life remains essential for their practical deployment. In commercial SIBs, hard carbon (HC) has emerged as the preferred anode material, while several classes of cathode material are being pursued, including layered transition-metal oxides, polyanionic compounds, and Prussian blue analogues [4,5]. Among these, layered $NaTMO_2$ cathodes, particularly Na–Fe–Mn (NFM) systems, e.g. $NaNi_{1/3}Fe_{1/3}Mn_{1/3}O_2$, stand out as highly successful and widely used active materials for commercial SIBs owing to their suitable capacities, operating potentials, and scalable synthesis [6,7]. These cathodes consist of alternating transition-metal oxide slabs, with sodium residing in the interlayer space. Depending on the composition and the sodiation state, NFM can exist in different stacking sequences during cycling. At high sodium contents, $NaNi_{1/3}Fe_{1/3}Mn_{1/3}O_2$ adopts an O3-type structure with octahedrally coordinated sodium ions and three repeated transition-metal layers per unit cell. Upon charging and progressive desodiation, the material undergoes a phase transition to a prismatic P-type structure [8]. The O3 to P3 phase transition is reported to be highly reversible, allowing stable cycling within a moderate voltage range of approximately 2.0 V to 4.0 V vs. Na^+/Na [9]. However, at elevated upper cut-off voltages, corresponding to deep desodiation states, additional structural transformations can occur. In particular, transitions from P3 to distorted high-voltage phases have been reported, described in the literature as O3′ [10,11], P3′, OP2 [9,12] or combinations thereof [13]. These high-voltage phase transitions are typically associated with increased lattice strain [14] and can, upon repeated cycling, induce cumulative structural damage, impedance growth, and accelerated capacity fade. Such voltage-induced degradation phenomena have already been demonstrated for layered NFM-based cathodes in half cells [9–12,15] and full-cell configurations [16–19], where operation at elevated upper cut-off voltages led to pronounced capacity decay and increased cell resistance over extended cycling. These studies highlight that structural instability of the cathode at high potentials directly translates into measurable cell aging. From an engineering perspective, commercial cells are required to be operated within a manufacturer-specified voltage window, while the onset of detrimental structural transitions under practical operating conditions is often not directly known for the specific cell design. In our previous work [19], we demonstrated that the occurrence and onset of detrimental phase transitions depend on the operating conditions. Thus, identifying the upper cut-off voltage at which the undesired high-voltage phase transition is initiated under different operating conditions is crucial for reliable cell operation. Once this onset is known, operating strategies can be developed to avoid or reduce cycling in the critical regime, for example by limiting or dynamically adapting the upper cut-off voltage during operation. However, the downside of lowering this voltage limit is that it reduces accessible energy and capacity, as it restricts the usable charge-storage window of the cell. While such strategies may improve cycle life and long-term electrochemical stability, they do so at the expense of energy and capacity. The operation of commercial NFM | HC sodium-ion cells therefore represents a multi-objective engineering problem in which energy, capacity, and cycle life must be balanced.

In this work, the electrochemical behavior of a commercially available cylindrical NFM | HC sodium-ion cell is first systematically investigated from this engineering perspective under different operating conditions, including temperature and C-rate. Particular emphasis is placed on identifying the upper cut-off voltages at which the high-voltage phase transition in the layered NFM cathode is initiated. The structural changes accompanying this transition are monitored by operando X-ray diffraction (operando-XRD), providing a direct link between electrochemical behavior and structural evolution during cycling. The identified onset of this phase transition can therefore serve as a reference for selecting application-relevant upper cut-off voltages. Second, based on this transition-specific definition of the voltage-window, the impact of the selected upper cut-off voltage on engineering-relevant metrics, such as capacity, energy, and power capability, is assessed. Furthermore, long-term cycling tests are performed at different upper cut-off voltages to evaluate the influence of the voltage window on long-term performance. In particular, the study investigates whether operation below the onset of the high-voltage phase transition can improve cycling stability. This enables a quantitative evaluation of the trade-off between available capacity, energy, and high-voltage-induced degradation. Third, the results are used to assess whether an adjustment of the upper cut-off voltage as a function of operating conditions using a look-up table could provide a suitable basis for application-specific operation strategies. Additionally, a possible voltage-boosting strategy is discussed, in which the upper cut-off voltage is temporarily extended to balance higher capacity and energy output against long-term stability. This means that a higher upper cut-off voltage would be applied only temporarily, before returning to a more moderate voltage window for stable long-term cycling. Overall, this study complements previous mechanistic investigations on NFM-based cathodes and commercial cells that have addressed high-voltage phase-transition behavior and associated aging mechanisms in greater detail. In contrast, the present work establishes an application-oriented framework that links the onset of the high-voltage phase transition to practical voltage-window selection, quantifies the trade-off between energy availability and cycling stability, and derives application-specific operating strategies for commercial sodium-ion cells. The key contributions of this work can be summarized as follows:

- Determination of the upper cut-off voltage at which the high-voltage phase transition is initiated under different operating conditions
- Systematic assessment of whether operation below the onset of this phase transition improves long-term cycling stability
- Quantification of the trade-off between available energy, reversible capacity, and long-term degradation as a function of the applied upper cut-off voltage
- Establishment of application-specific operating strategies, including phase transition avoidance for lifetime-oriented operation and temporary extension of the upper cut-off voltage for energy boosting

2. Identification of cathode phase transitions during electrochemical cycling

Cathode phase transitions during electrochemical cycling can strongly affect the voltage response and accessible capacity of commercial cells, yet their identification is challenging when only

Table 1
Test sequences of the C-rate tests.

Cycle	Charging	Discharging
1	0.2C	0.2C
2	0.05C	0.05C
3	0.2C	0.5C
4	0.2C	0.2C
5	0.2C	0.2C
6	0.2C	1C
7	0.2C	2C
8	0.2C	0.2C
9	0.5C	0.2C
10	1C	0.2C
11	2C	0.2C

electrochemical data are considered. Therefore, incremental capacity analysis (ICA) and operando-XRD are combined to identify phase transition features under different operating conditions and to assign them unambiguously to structural changes in the cathode material. The following section first introduces the applied methodology and the investigated cell before presenting and discussing the experimental results.

2.1. Experimental techniques for phase transition analysis

Throughout this work, commercial 18 650 cells with a nominal capacity of 1.50 A h, manufactured by Shenzhen Zhonghuajia Technology Co., Ltd., Shenzhen, China, were used. The cells, including their cathode and anode active materials, served as the basis for all subsequent experiments and analyses. According to the manufacturer's datasheet, the cells can be cycled within a voltage range of 1.50 V to 4.10 V. Cells of the same type were already used and analyzed in other studies [20–25]. Bischof et al. [20] identified NFM as the cathode active material and HC as the anode active material.

2.1.1. C-rate tests

All cells underwent an initial cycling procedure at 25 °C before the subsequent C-rate tests were performed. During the initial cycling, the cells were charged with a constant current (CC) of 0.5C (refered to the nominal capacity of the cells, according to the manufacturer) until the upper voltage limit of 4.10 V was reached. The CC charging was followed by a constant voltage (CV) phase until a cut-off current of C/20 was reached. Subsequently, the cells were CC discharged at 0.5C. The discharge process was carried out in accordance with the manufacturer's datasheet without a CV phase. This procedure was repeated five times. For all cycling procedures an Arbin Instruments LBT21084 battery tester was used and the cells were placed in a Binder MK 115 climate chamber. The initial cycling was conducted at 25 °C. Subsequently, C-rate tests were conducted at three different temperatures (10 °C, 25 °C and 40 °C). To ensure defined environmental conditions, the cells were equilibrated at the respective test temperature for 4 h prior to testing. The cells were then cycled using the protocol in Table 1 to ensure a uniform initial state before each charge or discharge step with the specified C-rates, the cells were first charged or discharged at a C-rate of 0.2C. Three cells were tested at each temperature.

2.1.2. C-rate tests with experimental cells

To complement the C-rate tests on the commercial cells, experimental cells equipped with a reference electrode were assembled from active material recovered from an as-received commercial 18 650 cell, enabling the transfer of the same test protocol to a laboratory cell configuration. This approach allows the full-cell response to be deconvoluted into cathode- and anode-specific contributions. For this purpose, the 18 650 cell was opened in an argon-filled glovebox, the double side coated electrode sheets were extracted, and the active material coating was removed from one side of each electrode prior to further cell preparation. The experimental cells were assembled in an ECC-PAT-Core laboratory test cell setup (EL-Cell). Electrode discs with a diameter of 18 mm were mounted in a prefabricated separator/reference-ring unit supplied by EL-Cell, and each cell was filled with 100 µL of 1 M $NaPF_6$ in EC:DMC electrolyte, purchased from Sigma-Aldrich Chemie GmbH. To ensure sufficient wetting of the active material, the assembled cells were rested for at least 12 h at 25 °C in a climate chamber operated with a Huber CC-515 recirculating thermostat. The experimental cells were cycled using a Biologic VMP300 battery tester. Prior to the C-rate measurements, two formation cycles at 0.2C and one cycle at 0.5C were conducted to determine the cell capacity. The cells were then subjected to the same C-rate test protocol as applied to the commercial cells (see Table 1).

2.1.3. Operando-XRD measurement

To unambiguously identify the phase transitions occurring during electrochemical cycling, operando-XRD measurements were performed using a customized CR2032 coin cell with a 6 mm quartz glass window of 100 µm thickness. The cell was assembled using the same electrode material as introduced in the previous section. Electrode discs with diameters of 14 mm for the anode and 13 mm for the cathode were punched from the electrode sheets. A Whatman GF/A glass fiber separator was placed between the electrodes, and 100 µL of 1 M $NaPF_6$ in EC:DMC (1:1) was used as electrolyte. Following assembly, the cell was subjected to two formation cycles at C/20 and one cycle at 1C using a CCCV protocol to ensure that both the fully charged and fully discharged states were covered during the XRD measurements. Operando-XRD data were then collected during galvanostatic cycling in a voltage range from 1.50 V to 4.10 V at C/20 and 1C. Measurements were performed in transmission geometry on a Stoe Stadi P diffractometer (Mo–Kα_1 radiation (λ = 0.709 32 Å, 50 kV, and 40 mA)), with diffraction patterns recorded every 15 min at C/20 and every 5 min at 1C over a range of $0° \leq 2\theta \leq 36.5°$ using a step size of 0.015°.

2.1.4. Characterization methods

While operando-XRD enables the unambiguous identification of phase transitions during electrochemical cycling, valuable information can also be derived from electrochemical data. In particular, characteristic changes in the voltage profiles, when evaluated by differential methods such as ICA, can indicate the presence of phase transitions [26,27]. For this purpose, the incremental capacity, dQ/dV, is calculated from constant-current charge and discharge data and plotted as a function of cell voltage. Peaks in the resulting curves can be associated with distinct electrochemical processes [26,27], while changes in peak position, height, and width provide insight into reaction mechanisms and can additionally be used to assess aging-related effects such as loss of active material, loss of cyclable ions, and increasing polarization [28–32]. As phase transitions can be reflected by distinct features in the ICA curves, electrochemical voltage data can provide clear indications of their occurrence. In combination with operando-XRD results, these features can then be assigned unambiguously to specific phase transitions and subsequently used as markers in further electrochemical measurements. In this work, the ICA data were processed using a tailored smoothing procedure to obtain sufficiently stable ICA curves for subsequent analysis. Prior to differentiation, the voltage and capacity data were smoothed using a Savitzky–Golay filter with a second-order polynomial [33] and a window length corresponding to 2 % of the recorded data points. For the experimental cell data, the calculated dQ/dV curves were additionally smoothed using a Savitzky–Golay filter with a window length corresponding to 4 % of the data points.

2.2. Analysis of the electrochemical behavior

The electrochemical response of the commercial SIB was first analyzed to identify characteristic voltage features. At 25 °C, the cell exhibits a pronounced high-voltage plateau at around 4.0 V during C/20

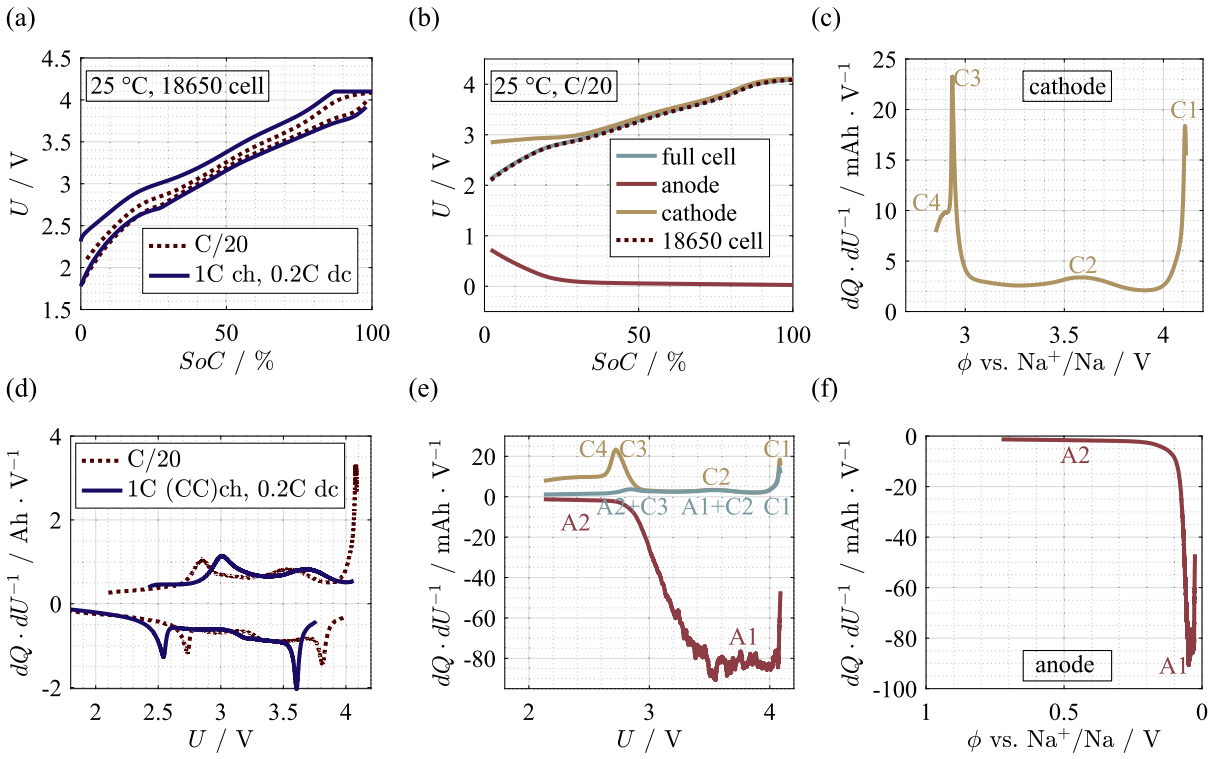


Fig. 1. Voltage curves during charging and discharging of a commercial 18 650 SIB at 25 °C in (a). (d) shows the corresponding IC data. Voltage profiles of the experimental cell during C/20 charging in (b), the corresponding IC curves in (e), and the individual IC curves of the cathode and anode in (c) and (f), respectively.

charging (Fig. 1(a)). In the corresponding IC curve (Fig. 1(d)), this feature appears as a sharp peak, reflecting the large amount of charge transferred within a narrow potential range [29]. At 1C, neither the voltage plateau in Fig. 1(a) nor the corresponding high-voltage peak in the IC curve in Fig. 1(d) is observed during the CC charging step. In the subsequent discharge, however, a corresponding high-voltage peak reappears in the IC curves for both charging conditions (Fig. 1(d)). After C/20 charging, this feature corresponds to the voltage region of the plateau observed during charge. After 1C charging, its reappearance during discharge, which was performed at 0.2C (see Table 1), suggests that the same high-voltage process is still accessed, although it is not resolved during the CC charging step and is likely completed only during the subsequent CV phase.

Since sharp features in IC curves are commonly associated with phase transitions [29], the origin of this high-voltage peak was investigated in more detail using experimental cells within a three-electrode setup. This approach allows the full-cell response to be separated into anode and cathode contributions and thereby enables assignment of the observed features to the responsible electrode. Fig. 1(b) and (e) show the voltage profiles and corresponding IC curves of the experimental cell cycled at C/20. The cathode IC curve in Fig. 1(c) exhibits four distinct peaks, including two pronounced features, C3 and C1, which coincide with plateau regions in the cathode potential profile (Fig. 1(b)) at the beginning and near the end of charge. The C4 peak may be attributed to the same electrochemical process as the C3 feature [34], while the broad, shallow C2 peak describes the intermediate SOC region, in which the cathode potential gradually increases between the two plateaus. In contrast, the anode IC curve in Fig. 1(f) is characterized by a broad plateau-like contribution between 0.8 V and 0.2 V (A2), followed by a shoulder-shaped feature (A1) below 0.2 V. If the anode and cathode contributions are plotted against full-cell voltage (Fig. 1(e)), three peaks can be distinguished in the resulting full-cell IC curve, consistent with the behavior observed for the commercial 18 650 cell (see Fig. 1(d)). The first peak during charge, denoted A2+C3, arises from the overlap of the cathode peak C3 with the plateau-like anode contribution A2. The second peak, A1+C2, likewise contains contributions from both electrodes, whereas the third high-voltage peak, C1, can be assigned exclusively to cathode processes.

2.3. Mapping of phase transitions trough operando-XRD and ICA

In previous studies [35], the C1 peak has been attributed to a phase transition from a P3 phase to a distorted O3′ phase. To confirm this phase transition and to unambiguously assign the C1 peak observed in the electrochemical data, operando-XRD measurements were performed at both C/20 and 1C. Fig. 2(a) to (d) presents the operando-XRD results obtained during C/20 charging and discharging of a coin cell assembled from the active material recovered from the commercial cell, together with the corresponding voltage profiles and ICA. This combination directly links the structural evolution to the electrochemical response. The overall diffraction contour plot in Fig. 2(a) [19] already indicates pronounced structural changes during cycling, while the corresponding voltage profile in Fig. 2(b) and the IC curves in Fig. 2(d) show that these changes coincide with the characteristic voltage plateau and the associated IC peaks. The enlarged view in Fig. 2(c) shows that the cathode first undergoes an O3 to P3 [16] transition during charging, which corresponds to the voltage region of the A2+C3 IC peak and thus to the cathode-related C3 feature identified by the three-electrode measurements. At higher voltages, further changes in the reflections coincide with the high-voltage C1 peak and indicate an additional structural transformation. However, the exact nature of this phase transition remains ambiguous. In earlier literature, it has been referred to as the formation of an O3′ phase [11],whereas later studies have described the high-voltage phase in terms of OP2 [9,12] or mixed structures [16]. Therefore, the notation O3′ should be understood as a phenomenological assignment rather than a definitive structural identification. Regardless of the exact structural assignment, these high-voltage phases are generally associated with reduced reversibility [9–

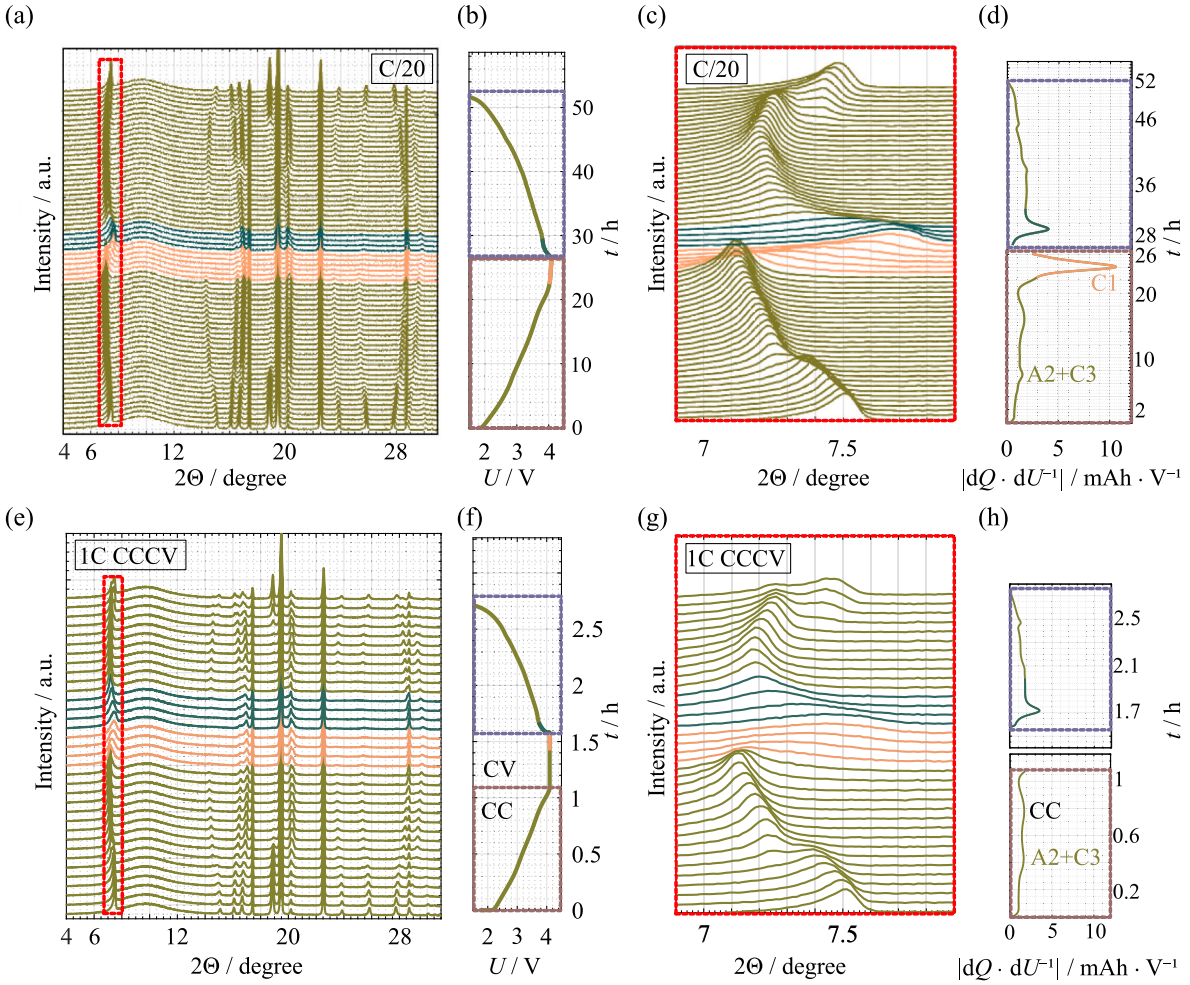


Fig. 2. Operando XRD results obtained during C/20 charging and discharging, as well as 1C CCCV charging and discharging of a coin cell containing the active material from the commercial cell. (a) Diffraction contour showing the structural evolution of the cell during C/20 cycling, (b) corresponding voltage profile, (c) enlarged view of the diffraction contour highlighting the region of pronounced structural changes in the NFM cathode, and (d) IC curves. (e) Diffraction contour showing the structural evolution of the cell during 1C cycling, (f) corresponding voltage profile, (g) enlarged view of the diffraction contour highlighting the region of pronounced structural changes in the NFM cathode, and (h) IC curves.

12,16]. In addition, the reverse reaction may be an asymmetric reaction in which an OP phase is formed, resulting in an additional phase transition from OP to P3 [36].

A comparison with the operando-XRD data obtained at 1C in Fig. 2(e) to (h) further reveals that the high-voltage transition already occurs during the CC step at C/20, whereas at 1C it is shifted to the subsequent CV phase. This rate-dependent behavior suggests that the occurrence of the transition is governed by the applied operating conditions. In the following, its appearance under different operating conditions is examined in more detail.

2.4. Influence of C-rate and temperature on the high-voltage phase transition

To identify the operating conditions under which the detrimental O3′ phase transition occurs, the IC curves obtained during charging at four C-rates (C/20, 0.2C, 0.5C, and 1C) and three temperatures (10 °C, 25 °C, and 40 °C) were evaluated. The IC curve recorded at 1C and 10 °C was excluded from the analysis, as sodium plating likely occurred under these conditions [21], altering the ICA features and rendering the curve unsuitable for evaluation. For each temperature, three cells were tested. For brevity, only one representative cell per condition is shown in the following, while the corresponding data for all cells are provided in Supplementary Figure S1. The IC curves of the CC charging step under the different operating conditions are presented in Fig. 3.

A fully developed C1 peak is observed only at C/20 and 25 °C as well as at C/20 and 0.2C at 40 °C, indicating that a pronounced O3′ phase transition occurs only under these conditions. At the adjacent conditions, namely C/20 at 10 °C, 0.2C at 25 °C, and 0.5C at 40 °C, the rising edge of the C1 peak is still discernible, suggesting that the O3′ phase transition is initiated but not fully developed. To determine the voltage up to which the onset of the phase transition can be reliably excluded, the local minimum of the IC curve following the A1+C2 peak is analyzed for all conditions. The robustness of the identified local minimum with respect to the applied smoothing procedure is evaluated in Supplementary Figure S2. The corresponding voltage threshold is governed by the overpotentials of the respective charging condition and ranges between 3.85 V (C/20, 40 °C) and 3.95 V (e.g. 0.5C, 25 °C). Therefore, 3.85 V was selected as a conservative upper cut-off voltage for all temperatures and C-rates, as it represents the lowest experimentally identified onset of the high-voltage phase transition within the investigated operating field. This ensures that the phase transition is avoided under all application-relevant test conditions considered in this study. Fig. 4 illustrates the impact of the voltage limit on the cell capacity, considering both a global cut-off voltage of 3.85 V and individually defined cut-off voltages based on the IC minimum as function of temperature and C-rate.

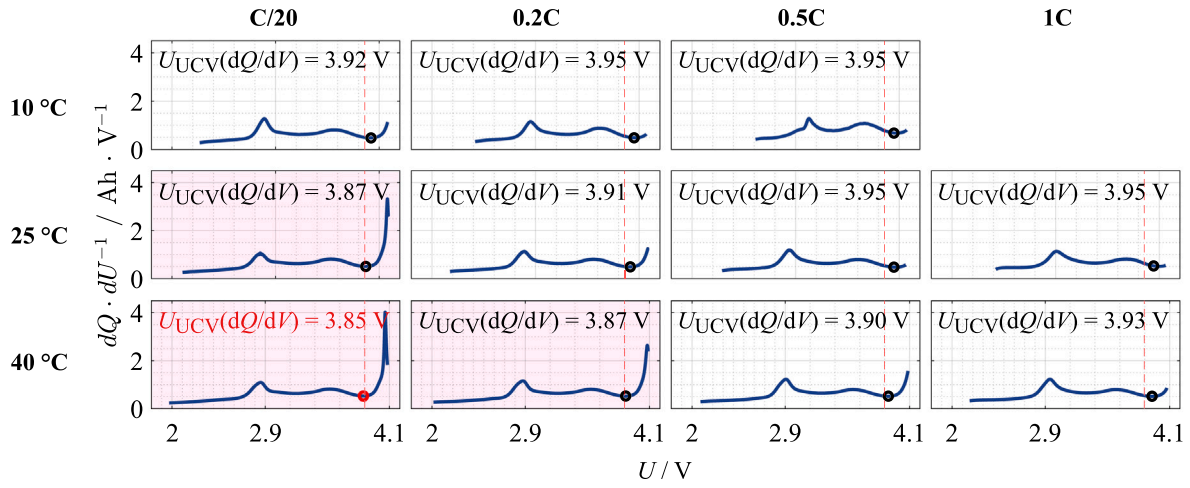


Fig. 3. IC curves obtained during the CC charging step under the investigated operating conditions. The local minima before the onset of the high-voltage phase transition indicate proposed IC-derived upper cut-off voltage limits, $U_{UCV}(dQ/dV)$. The dashed red vertical line indicates the global minimum among the proposed IC-derived upper-voltage limits at 3.85 V.

3. Analysis of the impact of upper cut-off voltages on performance

The choice of upper cut-off voltage directly affects the accessible operating window of the cell and therefore determines key performance metrics relevant for application such as capacity, energy, and pulse power capability. In this section, the influence of different upper cut-off voltages on these performance metrics is evaluated in order to quantify the benefit of a higher upper cut-off voltage and to assess the associated changes in cell performance.

3.1. Methodology for the determination of electrochemical performance metrics

The capacity and energy accessible within the different voltage windows were evaluated based on the C-rate tests by considering the corresponding cut-off voltages. Specifically, the charged capacity and charged energy are considered to quantify the amount of charge and energy stored within each voltage window. In addition, the pulse power capability is systematically assessed at 25 °C, enabling a consistent comparison between the investigated voltage windows. For this purpose, a pulse-current protocol was used, in which 1C current pulses were applied at defined SoC levels across the investigated operating range. The pulses were performed in 1 % SoC increments, with the step size determined from a preceding capacity measurement. The pulse power capability is evaluated following a Hybrid Pulse Power Characterization (HPPC)-based approach described by Belt [37]. For each SoC step, the 10 s resistance is determined from the voltage response during the current pulse relative to the quasi-equilibrium voltage measured directly before the pulse. For discharge pulses, the 10 s resistance is calculated according to

$$R_{dc,10\ s} = \frac{U_0 - U_{dc,10\ s}}{I_{dc}}, \tag{1}$$

where U_0 is the voltage directly before the pulse, $U_{dc,10\ s}$ is the cell voltage after 10 s of the discharge pulse, and I_{dc} is the applied discharge current. For charge pulses, the corresponding 10 s resistance is determined using

$$R_{ch,10\ s} = \frac{U_{ch,10\ s} - U_0}{I_{ch}}, \tag{2}$$

where $U_{ch,10\ s}$ is the cell voltage after 10 s of the charge pulse and I_{ch} is the absolute value of the applied charge current.

Based on the obtained 10 s resistances, the discharge pulse power capability is calculated using the lower cut-off voltage of the respective voltage window according to

$$P_{dc} = \frac{U_{min}\left(U_0 - U_{min}\right)}{R_{dc,10\ s}}, \tag{3}$$

while the charge pulse power capability is calculated using the upper cut-off voltage according to

$$P_{ch} = \frac{U_{max}\left(U_{max} - U_0\right)}{R_{ch,10\ s}}. \tag{4}$$

Here, U_{min} and U_{max} represent the lower and upper voltage limits of the investigated voltage window, respectively.

3.2. Analysis of the effect of upper cut-off voltage on capacity, energy, and pulse power

The highest capacity loss, reaching nearly 20 %, occurs under operating conditions that exhibit a pronounced O3′ phase transition, as shown in Fig. 4. At higher overpotentials, however, the relative capacity loss caused by lowering the upper cut-off voltage is less severe, indicating that individually adapted voltage limits are particularly advantageous in these cases. For instance, at 0.5C and 10 °C, approximately 6 % additional capacity remains accessible while still avoiding the phase transition. A similar trend is observed for the cell energy (see Supplementary Figure S3). In this case restricting the voltage window would lead to an even larger energy loss, with differences approaching 25 % in cases with a pronounced O3′ phase transition. In summary, the results indicate that individually adjusted voltage limits are especially beneficial at higher overpotentials, where they enable a better utilization of the available capacity without inducing the harmful phase transition. However, in operating conditions where the phase transition is strongly pronounced, avoiding it requires a substantial restriction of the voltage window, resulting in capacity losses of up to 20 %.

Fig. 5 shows the charge pulse power capability at 25 °C calculated for different upper cut-off voltages. Increasing the upper cut-off voltage from 3.85 V to 4.10 V results in a pronounced increase in the maximum charging pulse power capability. While the maximum pulse power is limited to 25.49 W for the 3.85 V cut-off voltage, it increases to 34.05 W when charging up to 4.10 V, corresponding to an improvement of approximately 33.6 %. Notably, the maximum pulse power capability of the cell is only reached after a charge throughput of approximately 0.4 A h. At the beginning of charging, the pulse power is limited by comparatively high 10 s resistance values, as shown in Supplementary Figure S4. A similar resistance behavior has also been reported in the literature [22,38,39]. The corresponding analysis of the discharge

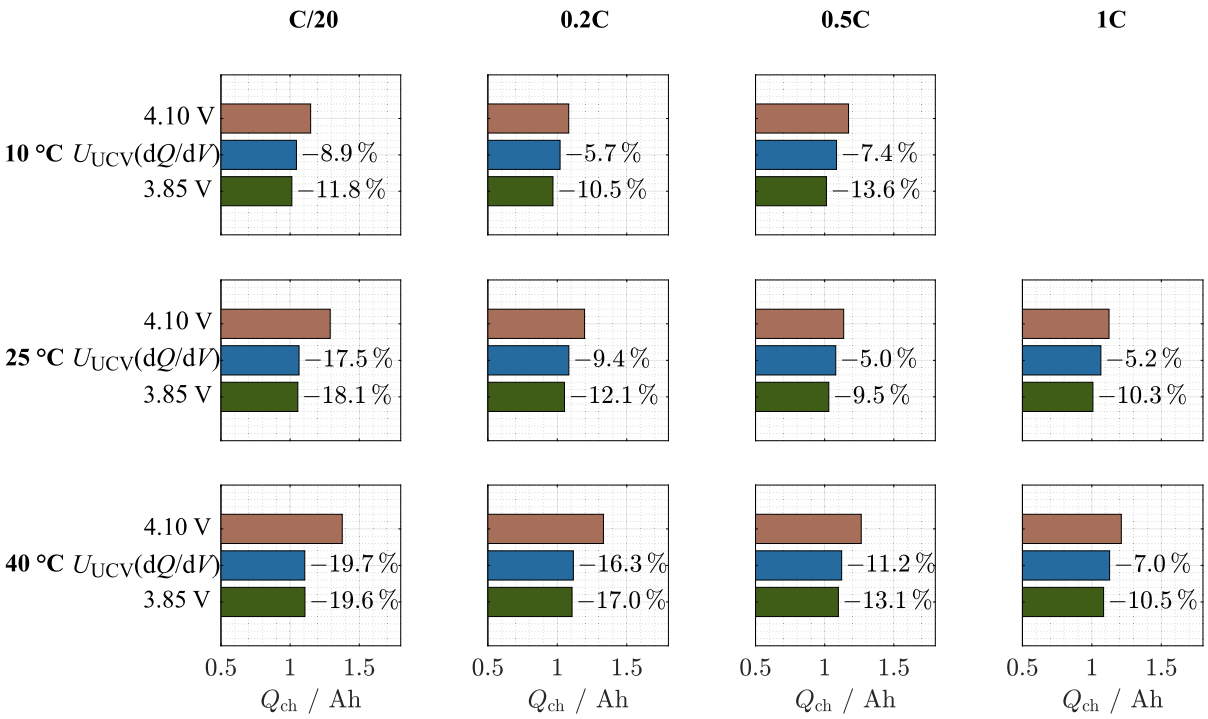


Fig. 4. Impact of the upper cut-off voltage on cell capacity, comparing a global cut-off voltage of 3.85 V with individually defined cut-off voltages derived from the IC minimum for each temperature and C-rate condition.

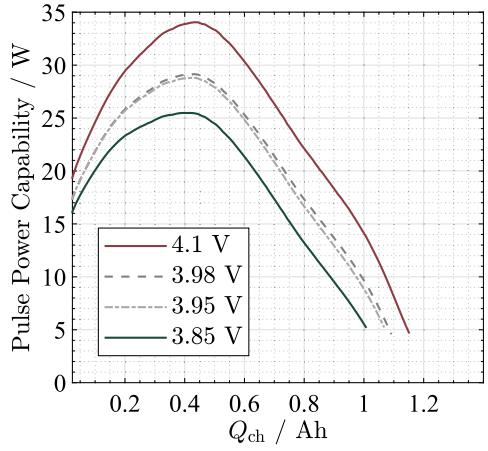


Fig. 5. Charge pulse power capability at 25 °C calculated for different upper cut-off voltages.

pulse power capability is provided in Supplementary Figure S5. As reducing the upper cut-off voltage entails a considerable performance loss, the following section investigates the impact of the high-voltage phase transition on cell aging. The aim is to evaluate whether the additionally accessible capacity outweighs the potential degradation effects associated with the O3′ phase transition or whether limiting the upper cut-off voltage provides an overall benefit.

4. Effects of upper cut-off voltages on aging and degradation analysis

To examine the effect of the upper cut-off voltage on aging, a long-term cycling study was conducted at three different voltage levels. With an elevated-temperature and a low C-rate, 0.2C and 40 °C, the test conditions were chosen to promote the phase transition at an upper cut-off voltage of 4.10 V and to exclude sodium metal deposition. This is because sodium metal deposition in hard-carbon SIBs is primarily associated with low-temperature charging, fast charging, and high current densities [21,40,41]. As a result, the observed differences in degradation can be interpreted primarily with respect to the effect of the upper cut-off voltage and the associated phase transition.

Table 2
Overview of the voltage windows used for long-term cycling.

Voltage window	Voltage range
Datasheet voltage range	1.50 V to 4.10 V
Intermediate upper cut-off	1.50 V to 3.98 V
Reduced upper cut-off	1.50 V to 3.85 V

4.1. Experimental procedure for long-term cycling tests

The cells used for the long-term cycling study underwent the same initial cycling procedure as those used in the C-rate test, described in Section 2.1. Afterward, they were characterized by a check-up test at beginning of life (BoL), which was repeated after every charge throughput of 120 A h and again at the end of the long-term cycling test. The check-up was conducted at 25 °C and included a pseudo-open-circuit voltage (pOCV) measurement at C/20, based on the nominal cell capacity, as well as electrochemical impedance spectroscopy (EIS) measurements at 0 %, 10 %, 50 %, and 80 % SoC, referenced to the capacity obtained from the BoL pOCV cycling. Following the initial characterization, long-term cycling was performed at 40 °C using three different voltage windows, with two cells tested per condition. To enable a systematic comparison of the influence of the upper cut-off voltage, the applied voltage ranges are summarized in Table 2. For all cells, the cycling rate was set to 0.2C with respect to the measured pOCV capacity at BoL.

The cells cycled between 1.50 V and 3.98 V were subjected to a reduced check-up protocol without EIS measurements.

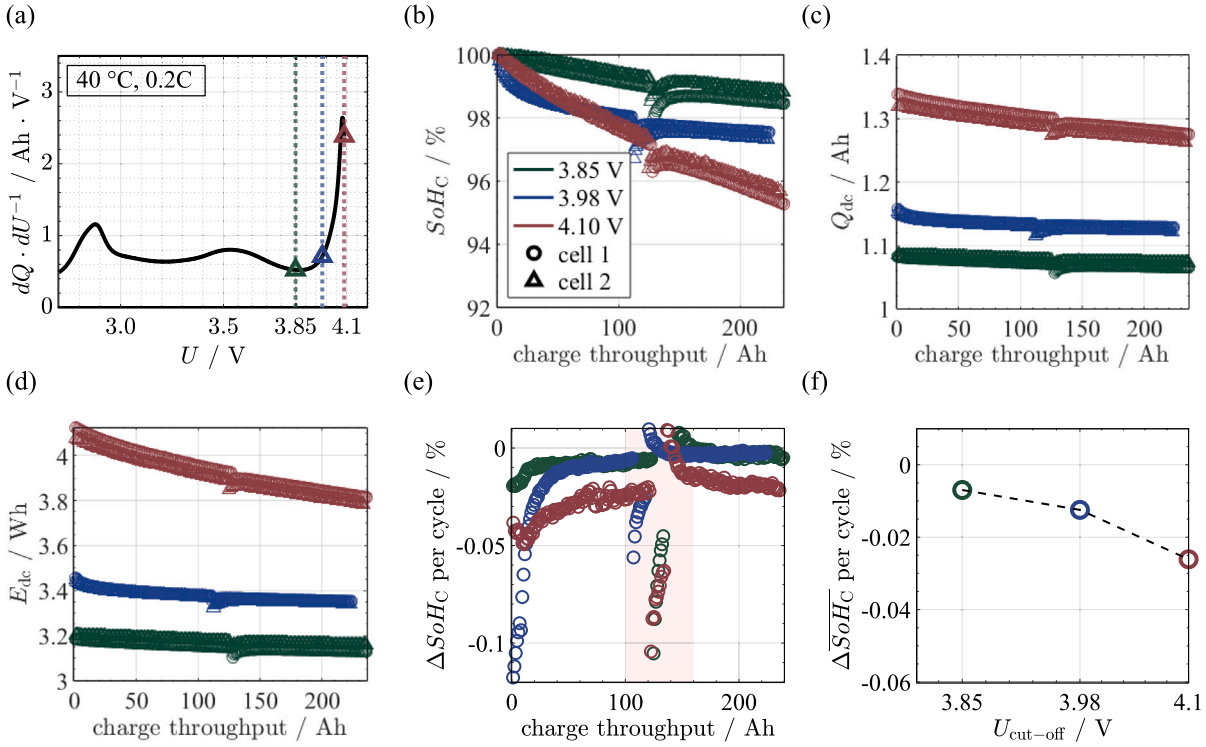


Fig. 6. Degradation behavior of cells cycled at different upper cut-off voltages at 0.2C and 40 °C. (a) Selected upper cut-off voltages in the IC curve. (b) Evolution of SoH_C as a function of charge throughput, calculated from the charged capacity, for two cells per condition. (c,d) Discharge capacity and energy over charge throughput. (e) Cycle-to-cycle difference in SoH_C for one representative cell per condition; a moving average over 10 cycles was applied. The red-marked region indicates distortion caused by the check-up cycle. (f) Mean ΔSoH_C for the three investigated cases. (For interpretation of the references to color in this figure legend, the reader is referred to the web version of this article.)

4.2. Effect of upper cut-off voltage on aging

Fig. 6(a) shows the three selected upper cut-off voltages in the IC analysis: the manufacturer-specified cut-off voltage of 4.10 V, the cut-off voltage of 3.85 V that does not lead to the phase transition as identified in Section 2.4, and the intermediate voltage between these two values, 3.98 V.

Fig. 6(b) presents SoH_C as a function of charge throughput, calculated from the charged capacity, for two cells per upper cut-off voltage. The capacity-based SoH SoH_C, is the ratio of the present cell capacity to the capacity of the cell at BoL [42,43]

$$SoH_C = \frac{Q_{dc,i}}{Q_{dc,BoL}} \tag{5}$$

A clear dependence on the upper cut-off voltage is observed. The 4.10 V cells exhibit the strongest capacity fade and consequently the most rapid decrease in SoH_C, whereas the 3.85 V cells show only minor degradation over the investigated charge throughput. The 3.98 V cells display a pronounced initial decrease in SoH_C. However, after approximately 50 cycles, their aging trajectory intersects with that of the 4.10 V case and subsequently remains closer to the 3.85 V cut-off voltage behavior. The check-up at a charge throughput of around 120 A h causes substantial changes in the curves for several subsequent cycles, after which the curves return to approximately their previous shape. The underlying reasons for this transient behavior remain unclear and require further investigation.

While the higher upper cut-off voltage leads to faster degradation, Fig. 6(c) and (d) show that the 4.10 V case still provides a substantially higher absolute capacity and energy. Importantly, even after a charge throughput of 240 A h, no intersection with the lower-voltage cases is observed. Thus, despite the accelerated SoH_C loss, the 4.10 V operating window remains advantageous in terms of accessible capacity and energy within the investigated aging range. This indicates that such an operating strategy may still be suitable for applications in which high capacity and energy are prioritized over cycle life, especially for use cases where only a limited number of cycles is required.

Fig. 6(e) shows the cycle-to-cycle difference in SoH_C as a function of charge throughput for one representative cell per upper cut-off voltage. For improved clarity, a moving average over 10 cycles was applied to the data. The 3.98 V case exhibits a higher initial loss in SoH_C than the 4.10 V case, despite its higher accessible capacity and energy. However, this increased loss is limited to the early stage of aging. In the region marked in red, the results are affected by the check-up cycle and are therefore of limited interpretability. In all cases, the degradation is initially elevated before approaching a more constant level, with the 3.85 V case reaching this steady behavior most rapidly. The faster stabilization observed for the 3.85 V case suggests that early-cycle changes are less pronounced under the reduced upper cut-off voltage, allowing the degradation rate to approach a quasi-steady-state regime more rapidly. The intermediate 3.98 V case, appears to retain a significant part of the capacity and energy benefit without showing a continuously elevated incremental degradation. From an application-oriented perspective, this behavior is particularly relevant, as it points towards a potentially advantageous trade-off between performance and lifetime. Although the 4.10 V case exhibits the largest loss in SoH_C, the degradation rate decreases over cycling and eventually approaches a nearly constant level. This indicates that, despite the stronger degradation, the cell does not continue to degrade progressively faster, but rather reaches a stable aging regime while still offering the highest accessible capacity and energy. Fig. 6(f) presents the mean ΔSoH_C for the three investigated cases. The elevated mean value of the 3.98 V case compared to the 3.85 V is primarily caused by the pronounced initial losses. To support the interpretation of the degradation results, a brief analysis based on ICA is presented in the following. This approach enables a more detailed assessment of the electrochemical changes associated with cycling at different upper cut-off voltages.

4.3. Analysis of degradation modes

For the 4.10 V case, Fig. 7(a) shows the ICA data of all charging cycles as a function of charge throughput. The characteristic peaks, which were assigned based on Fig. 1, are marked accordingly. With increasing charge throughput, an increase in the peak height of the A2+C3 peak can be observed, as shown in Fig. 7(d). This behavior indicates a cathode-related degradation. A loss of accessible desodiated cathode active material reduces the usable capacity of the full cell and therefore effectively compresses the cathode OCV profile along the capacity axis. As a consequence, cathode-related features in the full-cell IC curve are shifted on the voltage axis relative to the anode features. In the present case, the C3 peak moves closer to the flank of the A1/A2 anode feature, leading to a stronger overlap of both contributions (for the feature positions at BoL, see Fig. 1(e)). Since the full-cell IC signal reflects the superposition of the anode and cathode half-cell responses, the overlap of diverging A1/A2 and C3 contributions increases the magnitude of the resulting full-cell feature, leading to a larger peak height of the combined A2+C3 contribution. Therefore, the observed increase in peak height is consistent with a loss of accessible cathode active material. This interpretation is supported by Klick et al. who reported a similar peak evolution in a degradation mode analysis based on ICA [34], and by Lin et al. who demonstrated that elevated upper cutoff voltages promote the loss of participating cathode active material [16]. A schematic illustration of the proposed effect is provided in Supplementary Section 5. At the same time, the C1 peak is no longer fully covered during charging, until only its flank remains within the accessed voltage range. This trend can also be seen in the decreasing maximum C1 peak height in Fig. 7(b).

A possible reason for this behavior is an increase in cell resistance. In particular, an increase in charge-transfer resistance is supported by the EIS measurements performed during the check-up cycles, as shown in Supplementary Figure S7. Beyond the overall increase in cell resistance, some qualitative features of the EIS spectra are in line with the degradation trends inferred from the IC-based analysis. In particular, the aged 4.10 V case exhibits a more pronounced increase in semicircle diameter than the cells cycled at lower upper cut-off voltages. After a charge throughput of 240 A h, the corresponding spectrum may also indicate the onset of two distinguishable semicircle contributions. However, due to the overlap of the individual impedance contributions, a definitive assignment of these features to specific degradation processes is not possible based on the present data alone. A qualitatively similar impedance evolution dependent on the upper cut-off voltage was reported by Ye et al. who observed two overlapping semicircles for aged cells cycled to 3.9 V and 4.0 V, whereas only one semicircle for the 3.8 V case [18]. Ye et al. suggested that these contributions may be associated with increased contact resistance within the electrodes, for example as a result of particle cracking or the disconnection of active material, as well as with charge-transfer-related impedance at the electrode/electrolyte interface caused by the formation of a resistive surface layer during high-voltage degradation of the layered oxide positive electrode material [18]. An increase in semicircle size under high-voltage cycling conditions was also reported by Zhang et al. for sodium-ion pouch cells [17]. For the 3.98 V (see Fig. 7(e) to (g)) and 3.85 V (see Fig. 7(h) to (j)) cut-off voltage cases, the IC curves over charge throughput show only a minor increase in the height of the A2+C3 peak. This indicates that the loss of accessible cathode active material is less pronounced compared to the 4.10 V case. Furthermore, the increase in peak height is slightly smaller for the 3.85 V case (see Fig. 7(i)) than for the 3.98 V case (see Fig. 7(g)), suggesting that the extent of cathode-related degradation is lowest at the lowest upper cut-off voltage. The observed degradation effects in the 4.10 V case may primarily originate from the loss of accessible cathode active material, since a loss of cyclable sodium or sodiated anode material would be expected to manifest as a decrease in the A2+C3 peak [34]. However, enhanced anode-related degradation at the 4.10 V cut-off cannot be excluded completely, as HC anodes in SIBs are susceptible to interfacial degradation and sodium plating under conditions promoting deep anode sodiation [44].

5. Development of operating strategies

The long-term cycling results show that higher upper cut-off voltages accelerate cell aging while providing access to additional capacity associated with the phase transition. The following section briefly introduces possible operating strategies dealing with this behavior, focusing on the trade-off between lifetime requirements and temporary or condition-dependent access to higher capacities. These strategies are presented as conceptual operating approaches and are intended to provide a basis for future studies on their long-term aging impact and practical implementation.

5.1. Adaption of upper cut-off voltage as function of temperature and C-rate

The stronger capacity fade of the 4.10 V condition with increasing charge throughput was already evident from the SoH_C evolution shown in Fig. 6(b). Since practical lifetime requirements for stationary storage systems are commonly expressed in terms of full equivalent cycles (FEC) until an end-of-life criterion is reached, the discharge capacity was additionally evaluated as a function of FEC in Supplementary Figure S8. Stationary battery energy storage systems are commonly expected to reach several thousand FEC before 80 % SoH_C, with approximately 6000 FEC over 20 years reported for residential home storage systems [45,46]. Although Supplementary Figure S8 (a) only covers the experimentally investigated FEC range, the 4.10 V condition already exhibits a comparatively steep capacity decline. To qualitatively assess the implications for application-relevant lifetimes beyond the experimentally accessible cycle range, an illustrative proof-of-concept extrapolation of the observed capacity fade is provided in Supplementary Figure S8 (b). The extrapolation is based on an empirical fit and assumes that the experimentally observed degradation trend continues unchanged, i.e., without changes in the dominant aging mechanism or rollover behavior. It is therefore intended to illustrate the possible long-term trend rather than to provide a quantitative lifetime prediction. Details of the fitting procedure are provided in the Supplementary Information. Within these assumptions, the extrapolation indicates that the initial advantage of a higher capacity obtained by cycling up to 4.10 V would be lost after approximately 2000 FECs, where the remaining capacity approaches that of the 3.85 V condition. Furthermore, the 4.10 V condition is projected to reach the 80 % SoH_C criterion even earlier. Although the quantitative cycle numbers should be interpreted with caution, continuous operation up to 4.10 V would not meet typical lifetime expectations for stationary storage applications, despite the initially higher accessible capacity. In contrast, limiting the upper cut-off voltage to 3.85 V, and thereby avoiding the O3′ phase transition, is projected to provide sufficient cycling stability for such applications. While this confirms the relevance of a reduced voltage limit for long-term operation, a fixed conservative cut-off voltage may also leave part of the accessible capacity unused under certain operating conditions. Therefore, a more flexible strategy would be to define the upper cut-off voltage as a function of temperature and C-rate. This approach is based on the observation that the onset of the O3′ phase transition does not occur at a fixed applied voltage, but is shifted by overpotential contributions, as shown in Fig. 3. Consequently, the same upper cut-off voltage can correspond to different electrochemical states depending on the operating conditions. As a result, a conservative fixed cut-off voltage of 3.85 V may prevent the high-voltage phase transition under all conditions, but may also leave accessible capacity unused in operating regimes with higher overpotentials (see Fig. 4). Therefore, the phase transition onset identified by ICA in Fig. 3 can serve as a basis for defining condition-specific upper cut-off voltages. These voltage limits could be selected such that the O3′ phase transition is avoided for the respective temperature and C-rate, while additional capacity is accessed whenever the overpotential allows a higher applied cut-off voltage. One potential implementation of this concept would be to adjust the permissible upper cut-off voltage according to cell temperature and charging

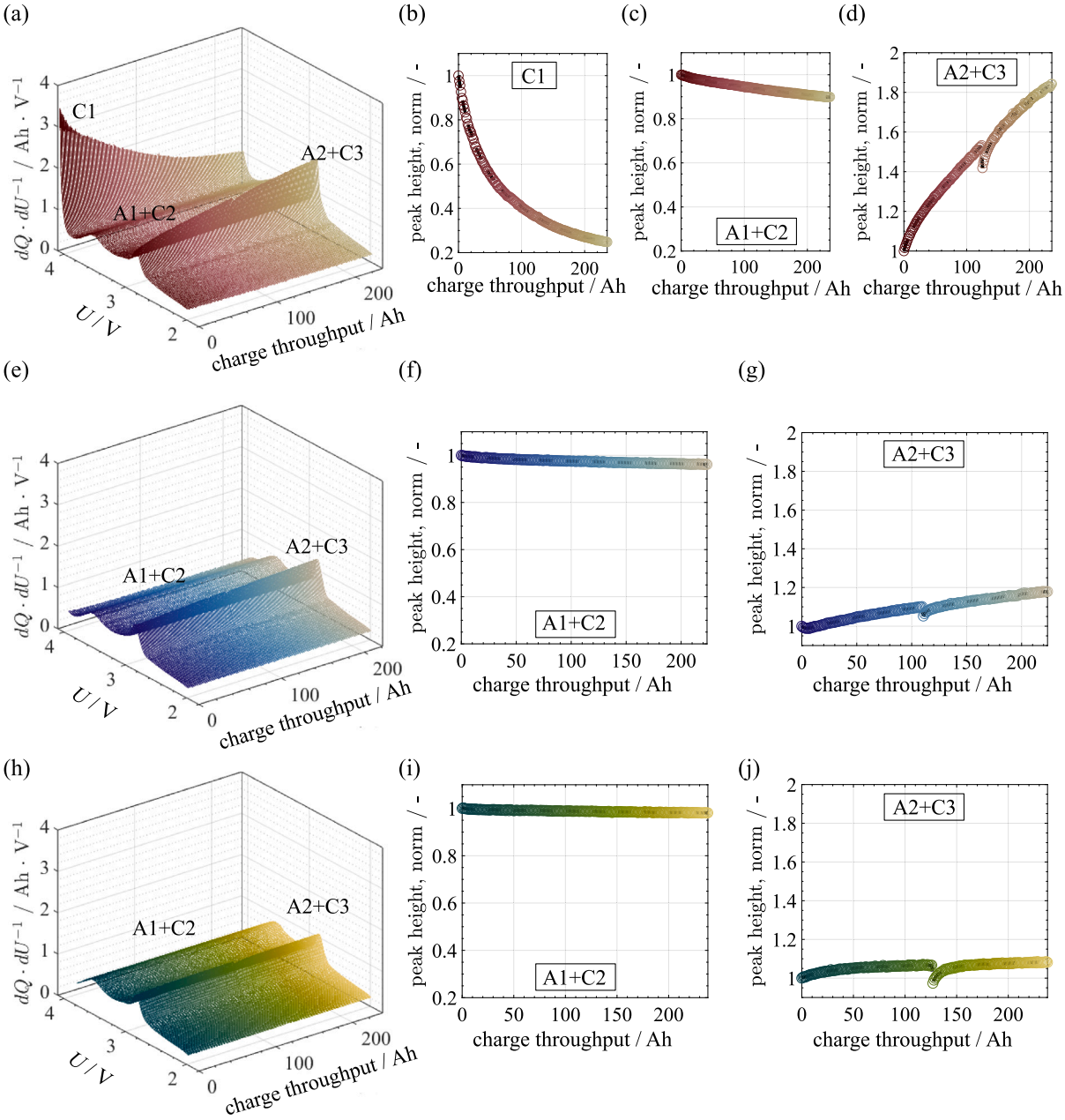


Fig. 7. Evolution of the IC features during long-term cycling for the different upper cut-off voltage cases. For the 4.10 V case, (a) shows the IC curves of all charging cycles as a function of cumulative charge throughput, while (b) to (d) show the normalized peak-height evolution of the C1, A1+C2, and A2+C3 peaks, respectively. The peak heights were normalized to their initial values obtained in the first cycle. Analogously, (e) shows the IC curves for the 3.98 V case, with the corresponding normalized evolution of the A1+C2 and A2+C3 peaks shown in (f) and (g). For the 3.85 V case, (h) shows the IC curves, while (i) and (j) show the normalized peak-height evolution of the A1+C2 and A2+C3 peaks, respectively.

C-rate, for example using a look-up table based on the experimentally identified phase-transition thresholds shown in Fig. 3. Such an adaptive strategy could increase the accessible capacity under conditions with higher overpotentials while retaining a more conservative voltage limit when the phase-transition onset occurs at lower terminal voltages. The development of a comprehensive operating map and the validation of the resulting adaptive voltage-limit strategy under dynamic and application-relevant operating conditions require further investigation. Such validation could follow an approach analogous to that applied in Section 4, in which the influence of avoiding the O3′ phase-transition region on long-term cycling stability was assessed for the 0.2C and 40 °C condition. Based on these findings, the adaptive strategy is expected to reduce cathode active material loss and improve cycling stability by limiting operation within the O3′ phase-transition region. However, a comprehensive validation across the relevant temperature and C-rate range, including dynamic and application-relevant operating conditions, is required and remains subject to future work.

5.2. Alternating upper cut-off voltages in booster-type applications

While condition-dependent voltage limits aim to avoid the O3′ phase transition during regular operation, temporary capacity or power demands could be addressed by intermittently increasing the upper cut-off voltage. Such a flexible upper cut-off voltage strategy was recently demonstrated for lithium-ion batteries by Wang et al. [47], who showed that alternating between high and reduced upper voltage limits can provide a trade-off between energy availability and lifetime. Although

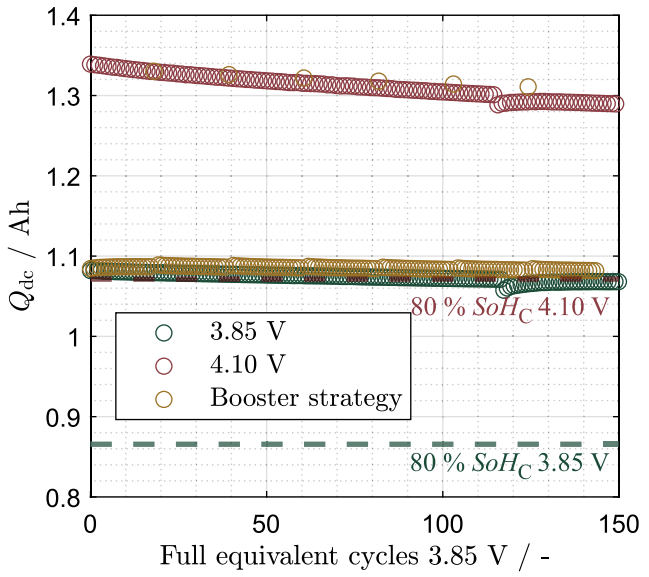


Fig. 8. Discharge capacity as a function of FEC for the booster-type cycling protocol compared to the fixed upper cut-off voltage cases. In the booster strategy, charging to 4.10 V was performed every 20th cycle, while the remaining cycles were limited to 3.85 V.

this approach was demonstrated for LIBs, the underlying principle is also relevant for SIBs, particularly when additional capacity becomes accessible at elevated upper cut-off voltages but continuous operation in this voltage range accelerates aging. Intermittent high-voltage operation may therefore provide a practical compromise between performance and degradation and is especially relevant for booster-type applications, where the additional capacity is accessed only temporarily when increased performance is required. To assess an intermittent high-voltage operation strategy representative of a booster application, an additional cycling test was performed based on the long-term cycling procedure described above. Two cells were cycled at 40 °C and 0.2C with respect to the pOCV capacity. While regular cycling was conducted between 1.50 V and 3.85 V, every 20th cycle was extended to an upper cut-off voltage of 4.10 V in order to temporarily access the additional high-voltage capacity. Fig. 8 shows the capacity evolution of the booster-type cycling protocol as a function of FEC, in comparison with the fixed cut-off voltage cases. The intermittent extension of the upper cut-off voltage to 4.10 V does not result in accelerated capacity fade compared to continuous cycling limited to 3.85 V. At comparable FEC numbers, the booster-type protocol also retains a higher discharge capacity than the cells cycled continuously up to 4.10 V. This indicates that a temporary, demand-driven increase of the upper cut-off voltage can provide access to additional high-voltage capacity without inducing the accelerated degradation observed during continuous high-voltage cycling. Thus, booster-type operation represents a promising strategy to exploit the performance benefit of the extended voltage window while maintaining cycling stability comparable to operation at the reduced upper cut-off voltage.

6. Conclusion

This work systematically investigated the influence of the upper cut-off voltage on the phase transition behavior, electrochemical performance, and degradation of commercial SIBs. By combining electrochemical analysis with operando structural characterization, the onset of the high-voltage phase transition was identified under different operating conditions. The results showed that the voltage at which the phase transition is initiated depends on the operating conditions applied, indicating that fixed voltage limits may not exploit the cell's full performance potential. Reducing the upper cut-off voltage below the onset of the high-voltage phase transition was found to improve long-term cycling stability. In particular, cycling limited to 3.85 V, at which the O3′ phase transition is avoided at 40°, resulted in significantly reduced capacity fade compared to continuous cycling up to 4.10 V. However, the higher upper cut-off voltage provided access to additional reversible capacity, energy and pulse power, highlighting the clear trade-off between performance and lifetime. The quantitative evaluation of capacity, energy, and pulse power capability demonstrated that extending the upper voltage limit can substantially enhance cell performance. Conversely, the long-term cycling results revealed that continuous operation in the high-voltage region accelerates degradation suggesting it may not be suitable for applications requiring high cycle stability, such as stationary energy storage. Therefore, the optimal upper cut-off voltage depends strongly on the intended application and the relative importance of energy availability, power capability, and lifetime. Based on these findings, two application-specific operating strategies can be derived. For applications focused on life-time, avoiding the high-voltage phase transition by limiting the upper cut-off voltage represents an effective approach to improve cycling stability. Since the onset of the phase transition depends on temperature and C-rate, the upper voltage limits can be defined according to the operating conditions, for example in a parameter table. This would improve capacity utilization while avoiding the phase transition region. In contrast, for applications that require additional energy or power only intermittently, temporarily extending the upper cut-off voltage provides access to the additional high-voltage capacity without causing the accelerated aging observed during continuous high-voltage cycling. Thus, the results provide a basis for adaptive voltage-window strategies that balance performance and lifetime in commercial SIBs.

CRediT authorship contribution statement

Andrea Kinberger: Writing – review & editing, Writing – original draft, Visualization, Validation, Methodology, Formal analysis, Data curation, Conceptualization. **Tom Rüther:** Writing – review & editing, Validation, Supervision, Methodology, Conceptualization. **Niklas Feistel:** Writing – review & editing, Data curation. **Qingsong Wang:** Writing – review & editing, Supervision, Data curation. **Matteo Bianchini:** Writing – review & editing, Supervision. **Michael A. Danzer:** Writing – review & editing, Validation, Supervision, Methodology, Conceptualization.

Declaration of competing interest

The authors declare that they have no known competing financial interests or personal relationships that could have appeared to influence the work reported in this paper.

Acknowledgments

Support by the BayBatt Cell Technology Center, funded by the Deutsche Forschungsgemeinschaft (DFG, German Research Foundation) - INST 91/452-1 LAGG, is gratefully acknowledged. Funded by the Open Access Publishing Fund of the University of Bayreuth. In order to improve the readability and language quality of this manuscript, ChatGPT by OpenAI and Writer by DeepL were utilized during the writing process. It is important to note that the content and ideas presented in the manuscript were not generated by these language models and the authors take full responsibility for the content. The color palette used in this report was developed by Crameri et al. [48] and is publicly available on Zenodo (https://doi.org/10.5281/zenodo.8035877).

Appendix A. Supplementary data

Supplementary material related to this article can be found online at https://doi.org/10.1016/j.jpowsour.2026.241076.

Data availability

Data will be made available on request.

References

[1] C. Vaalma, D. Buchholz, M. Weil, S. Passerini, A cost and resource analysis of sodium-ion batteries, Nat. Rev. Mater. 3 (4) (2018) http://dx.doi.org/10.1038/natrevmats.2018.13.

[2] R. Yokoi, R. Kataoka, T. Masese, V. Bach, M. Finkbeiner, M. Weil, M. Baumann, M. Motoshita, Potentials and hotspots of post-lithium-ion batteries: Environmental impacts and supply risks for sodium- and potassium-ion batteries, Resour. Conserv. Recycl. 204 (2024) 107526, http://dx.doi.org/10.1016/j.resconrec.2024.107526.

[3] A. Yao, S.M. Benson, W.C. Chueh, Critically assessing sodium-ion technology roadmaps and scenarios for techno-economic competitiveness against lithium-ion batteries, Nat. Energy 10 (3) (2025) 404–416, http://dx.doi.org/10.1038/s41560-024-01701-9.

[4] X. Xiang, K. Zhang, J. Chen, Recent advances and prospects of cathode materials for sodium-ion batteries, Adv. Mater. (Deerfield Beach Fla.) 27 (36) (2015) 5343–5364, http://dx.doi.org/10.1002/adma.201501527.

[5] S. Zhao, Z. Guo, K. Yan, X. Guo, S. Wan, F. He, B. Sun, G. Wang, The rise of prussian blue analogs: Challenges and opportunities for high–performance cathode materials in potassium–ion batteries, Small Struct. 2 (1) (2021) http://dx.doi.org/10.1002/sstr.202000054.

[6] M.H. Han, E. Gonzalo, G. Singh, T. Rojo, A comprehensive review of sodium layered oxides: powerful cathodes for Na-ion batteries, Energy Environ. Sci. 8 (1) (2015) 81–102, http://dx.doi.org/10.1039/c4ee03192j.

[7] L. Li, Y. Zhang, B. Chen, J. Fan, X. Hu, Z. Liu, J. Huang, Z. Chen, K. Zou, Precursor microstructure regulation via co-precipitation: Unlocking balanced electrochemical performance of O3-type layered sodium cathode, Chin. Chem. Lett. (2026) 112755, http://dx.doi.org/10.1016/j.cclet.2026.112755.

[8] A. Namazbay, M. Karlykan, L. Rakhymbay, Z. Bakenov, N. Voronina, S.-T. Myung, A. Konarov, Towards high-performance sodium-ion batteries: A comprehensive review on Na Ni Fe Mn1−(+)O2 cathode materials, Energy Storage Mater. 77 (2025) 104212, http://dx.doi.org/10.1016/j.ensm.2025.104212.

[9] M. Jeong, H. Lee, J. Yoon, W.-S. Yoon, O3-type NaNi1/3Fe1/3Mn1/3O2 layered cathode for Na-ion batteries: Structural evolution and redox mechanism upon Na (de) intercalation, J. Power Sources 439 (2019) 227064, http://dx.doi.org/10.1016/j.jpowsour.2019.227064.

[10] X. Zhao, L. Zhang, X. Wang, J. Li, L. Zhang, D. Liu, R. Yang, X. Jin, M. Sui, P. Yan, Deciphering cycling voltage-dependent failures of O3-layered cathode for sodium ion battery, J. Mater. Chem. A 12 (19) (2024) 11681–11690, http://dx.doi.org/10.1039/d3ta07967h.

[11] Y. Xie, H. Wang, G. Xu, J. Wang, H. Sheng, Z. Chen, Y. Ren, C.-J. Sun, J. Wen, J. Wang, D.J. Miller, J. Lu, K. Amine, Z.-F. Ma, In operando XRD and TXM study on the metastable structure change of NaNi 1/3 Fe 1/3 Mn 1/3 O 2 under electrochemical sodium–Ion intercalation, Adv. Energy Mater. 6 (24) (2016) http://dx.doi.org/10.1002/aenm.201601306.

[12] J. Lamb, L. Stokes, A. Manthiram, Delineating the capacity fading mechanisms of Na(Ni 0.3 Fe 0.4 Mn 0.3)O 2 at higher operating voltages in sodium-ion cells, Chem. Mater. 32 (17) (2020) 7389–7396, http://dx.doi.org/10.1021/acs.chemmater.0c02292.

[13] R. Liu, S. Yang, S. Zhou, J. Xing, X. Niu, G. Pang, G. Liu, F. Ye, B. Xiao, C. Xu, Regulating reversible phase transition at high voltage window on O3-type layered cathodes by doping Zn for sodium-ion batteries, Small (Weinheim Bergstr. Ger.) 21 (37) (2025) e05197, http://dx.doi.org/10.1002/smll.202505197.

[14] Z. Xu, H. Yang, X. Zhao, R. Zheng, Z. Song, Z. Wang, H. Sun, Y. Liu, D. Wang, Suppressed P3-O3' phase transition and enhanced Na+ diffusion kinetics of O3-type layered oxide cathode via multivariate doping, ACS Appl. Mater. Interfaces 17 (1) (2025) 1085–1096, http://dx.doi.org/10.1021/acsami.4c16665.

[15] Y. Gan, H. Cui, K. Zhang, Y. Song, W. Gao, Exploring the degradation characteristics and thermal stability of NaNi1/3Fe1/3Mn1/3O2 cathode for sodium-ion battery cycling with high potential, J. Energy Storage 114 (2025) 115776, http://dx.doi.org/10.1016/j.est.2025.115776.

[16] S. Lin, W. Li, H. Yang, M. Chen, H. Xie, Y. Qin, J. Zeng, P. Zhang, J. Zhao, High-voltage cycling degradation mechanisms of the NaNi 1/3 Fe 1/3 Mn 1/3 O 2 cathode in sodium-ion pouch cells, EES Batter. 1 (4) (2025) 935–946, http://dx.doi.org/10.1039/d5eb00077g.

[17] R. Zhang, R. Wang, S. Gu, L. Huang, Y. Yan, G. Zhu, H. Zheng, Unravelling the failure mechanism of sodium ion pouch cell with layered cathode cycled under high voltage, J. Energy Storage 135 (2025) 118391, http://dx.doi.org/10.1016/j.est.2025.118391.

[18] Z. Ye, L. Zhang, H. Hijazi, B. Tang, Y. Zhang, S. Yu, H. Ni, B. Rutherford, J. Dahn, M. Metzger, The origin of high voltage degradation in O3-layered oxide/hard carbon sodium-ion pouch cells, J. Electrochem. Soc. 173 (1) (2026) 010506, http://dx.doi.org/10.1149/1945-7111/ae2f2e.

[19] T. Rüther, A. Kinberger, N. Feistel, M. Bianchini, M.A. Danzer, Excessive sodiation and desodiation of commercial NFM-hard carbon sodium-ion batteries induced by low-rate cycling, J. Power Sources Adv. 37 (2026) 100199, http://dx.doi.org/10.1016/j.powera.2025.100199.

[20] K. Bischof, V. Marangon, M. Kasper, A. Aracil Regalado, M. Wohlfahrt-Mehrens, M. Hölzle, D. Bresser, T. Waldmann, Evaluation of commercial 18650 and 26700 sodium-ion cells and comparison with well-established lithium-ion cells, J. Power Sources Adv. 27 (2024) 100148, http://dx.doi.org/10.1016/j.powera.2024.100148.

[21] K. Bischof, M. Feinauer, A. Aracil Regalado, M. Wohlfahrt-Mehrens, M. Hölzle, T. Waldmann, Sodium metal deposition in commercial sodium-ion cells, J. Electrochem. Soc. 172 (9) (2025) 090520, http://dx.doi.org/10.1149/1945-7111/ae0075.

[22] M. Rehm, M. Fischer, M.R. Gomez, M. Schütte, D.U. Sauer, A. Jossen, Comparing the electrical performance of commercial sodium-ion and lithium-iron-phosphate batteries, J. Power Sources 633 (2025) 236290, http://dx.doi.org/10.1016/j.jpowsour.2025.236290.

[23] V. Marangon, K. Bischof, A.A. Regalado, M. Keppeler, M. Pogosova, M. Wan, J. Choi, S. Fleischmann, T. Diemant, M. Wohlfahrt-Mehrens, M. Hölzle, T. Waldmann, D. Bresser, Cell design and chemistry of commercial sodium-ion battery cells, J. Power Sources 634 (2025) 236496, http://dx.doi.org/10.1016/j.jpowsour.2025.236496.

[24] B. Auch, C. Weisenberger, P. Kaya, V. Knoblauch, New insights into commercial 18650 sodium–Ion batteries: Understanding cell characteristics and ageing through multi method analyses, Batter. Supercaps 9 (3) (2026) http://dx.doi.org/10.1002/batt.202500925.

[25] B. Thilakarathna, D. Brocklebank, P.K.M. Tung, V.K. Peterson, N. Sharma, Commercial sodium–Ion batteries: Understanding mechanism and function using in operando neutron diffraction and X–ray tomography studies, Adv. Funct. Mater. 36 (6) (2026) http://dx.doi.org/10.1002/adfm.202510423.

[26] M. Dubarry, B.Y. Liaw, Identify capacity fading mechanism in a commercial LiFePO4 cell, J. Power Sources 194 (1) (2009) 541–549, http://dx.doi.org/10.1016/j.jpowsour.2009.05.036.

[27] A. Fly, R. Chen, Rate dependency of incremental capacity analysis (dQ/dV) as a diagnostic tool for lithium-ion batteries, J. Energy Storage 29 (2020) 101329, http://dx.doi.org/10.1016/j.est.2020.101329.

[28] M. Dubarry, C. Truchot, B.Y. Liaw, Synthesize battery degradation modes via a diagnostic and prognostic model, J. Power Sources 219 (2012) 204–216, http://dx.doi.org/10.1016/j.jpowsour.2012.07.016.

[29] M. Dubarry, D. Anseán, Best practices for incremental capacity analysis, Front. Energy Res. 10 (2022) http://dx.doi.org/10.3389/fenrg.2022.1023555.

[30] M. Safari, C. Delacourt, Aging of a commercial graphite/LiFePO4 cell, J. Electrochem. Soc. 158 (10) (2011) A1123, http://dx.doi.org/10.1149/1.3614529.

[31] C. Pastor-Fernández, K. Uddin, G.H. Chouchelamane, W.D. Widanage, J. Marco, A comparison between electrochemical impedance spectroscopy and incremental capacity-differential voltage as Li-ion diagnostic techniques to identify and quantify the effects of degradation modes within battery management systems, J. Power Sources 360 (2017) 301–318, http://dx.doi.org/10.1016/j.jpowsour.2017.03.042.

[32] Z. Ma, J. Jiang, W. Shi, W. Zhang, C.C. Mi, Investigation of path dependence in commercial lithium-ion cells for pure electric bus applications: Aging mechanism identification, J. Power Sources 274 (2015) 29–40, http://dx.doi.org/10.1016/j.jpowsour.2014.10.006.

[33] L. Li, Y. Li, W. Cui, Z. Chen, D. Wang, B. Zhou, D. Hong, A novel health indicator for online health estimation of lithium-ion batteries using partial incremental capacity and dynamic voltage warping, J. Power Sources 545 (2022) 231961, http://dx.doi.org/10.1016/j.jpowsour.2022.231961.

[34] S. Klick, H. Laufen, M. Schütte, B. Qian, K.L. Quade, C. Rahe, M. Dubarry, D.U. Sauer, Failure mode and degradation analysis of a commercial sodium–Ion battery with severe gassing issue, Batter. Supercaps 8 (4) (2025) http://dx.doi.org/10.1002/batt.202400546.

[35] Y. Xie, G.-L. Xu, H. Che, H. Wang, K. Yang, X. Yang, F. Guo, Y. Ren, Z. Chen, K. Amine, Z.-F. Ma, Probing thermal and chemical stability of Na x Ni 1/3 Fe 1/3 Mn 1/3 O 2 cathode material toward safe sodium-ion batteries, Chem. Mater. 30 (15) (2018) 4909–4918, http://dx.doi.org/10.1021/acs.chemmater.8b00047.

[36] N. Voronina, H.J. Kim, M. Shin, S.-T. Myung, Rational design of Co-free layered cathode material for sodium-ion batteries, J. Power Sources 514 (2021) 230581, http://dx.doi.org/10.1016/j.jpowsour.2021.230581.

[37] J.R. Belt, Battery test manual for plug-in hybrid electric vehicles, 2010.

[38] M. Rehm, J. Bahrke, J. Natterer, L. Milutinovic, F. Roehrer, A. Jossen, Aging of commercial sodium-ion batteries with layered oxides: how to measure and analyze it? EES Batter. 2 (2) (2026) 665–682, http://dx.doi.org/10.1039/D5EB00221D.

[39] S. Liu, K. Li, J. Yu, K. Liu, Characterisation and performance evaluation of early-generation commercial sodium-ion batteries, Appl. Energy 412 (2026) 127687, http://dx.doi.org/10.1016/j.apenergy.2026.127687.

[40] Y. Liu, L. Yang, R. Liao, Y. Zhang, S. Li, Study on low-temperature charging aging behavior and degradation mechanism of sodium-ion batteries, J. Energy Storage 124 (2025) 116927, http://dx.doi.org/10.1016/j.est.2025.116927.

[41] F. Liu, Z. Chen, Y. Li, L. Fu, J. Ju, J. Ma, Y. Sun, Sodium plating on hard carbon anodes in sodium-ion batteries: mechanisms, detection methods, and mitigation strategies, Nanoscale Horizons 11 (1) (2026) 62–84, http://dx.doi.org/10.1039/d5nh00471c.

[42] A. Farmann, W. Waag, A. Marongiu, D.U. Sauer, Critical review of on-board capacity estimation techniques for lithium-ion batteries in electric and hybrid electric vehicles, J. Power Sources 281 (2015) 114–130, http://dx.doi.org/10.1016/j.jpowsour.2015.01.129.

[43] T. Rüther, W. Hileman, M.S. Trimboli, G.L. Plett, M. Dubarry, N. Kumar, J. Marco, F. Roehrer, A. Jossen, J. Schöberl, M. Lienkamp, O. Bohlen, M.A. Danzer, Battery pack states, properties, and characterization techniques beyond cell level, Cell Rep. Phys. Sci. 6 (11) (2025) 102919, http://dx.doi.org/10.1016/j.xcrp.2025.102919.

[44] H. Hijazi, Z. Ye, L. Zhang, J. Deshmukh, M.B. Johnson, J.R. Dahn, M. Metzger, Impact of sodium metal plating on cycling performance of layered oxide/hard carbon sodium-ion pouch cells with different voltage cut-offs, J. Electrochem. Soc. 170 (7) (2023) 070512, http://dx.doi.org/10.1149/1945-7111/ace4fa.

[45] M. Naumann, R.C. Karl, C.N. Truong, A. Jossen, H.C. Hesse, Lithium-ion battery cost analysis in PV-household application, Energy Procedia 73 (2015) 37–47, http://dx.doi.org/10.1016/j.egypro.2015.07.555.

[46] M. Naumann, M. Schimpe, P. Keil, H.C. Hesse, A. Jossen, Analysis and modeling of calendar aging of a commercial LiFePO4/graphite cell, J. Energy Storage 17 (2018) 153–169, http://dx.doi.org/10.1016/j.est.2018.01.019.

[47] F. Wang, S. Tang, X. Han, Y. Wu, L. Lu, C. Yu, X. Sun, M. Ouyang, Flexible upper cut-off voltage regulation for life extension of lithium-ion batteries, Energy 318 (2025) 134776, http://dx.doi.org/10.1016/j.energy.2025.134776.

[48] F. Crameri, G.E. Shephard, P.J. Heron, The misuse of colour in science communication, Nat. Commun. 11 (1) (2020) 5444, http://dx.doi.org/10.1038/s41467-020-19160-7.